

1 **USING THE NAVIER-CAUCHY EQUATION FOR MOTION**
2 **ESTIMATION IN DYNAMIC IMAGING***

3 B.N. HAHN[†], M.-L. KIENLE-GARRIDO[†], C. KLINGENBERG[‡], AND S. WARNECKE[‡]

4 **Abstract.** Tomographic image reconstruction is well understood if the specimen being studied
5 is stationary during data acquisition. However, if this specimen changes during the measuring
6 process, standard reconstruction techniques can lead to severe motion artefacts in the computed
7 images. Solving a dynamic reconstruction problem therefore requires to model and incorporate
8 suitable information on the dynamics in the reconstruction step to compensate for the motion.

9 Many dynamic processes can be described by partial differential equations which thus could serve
10 as additional information for the purpose of motion compensation. In this article, we consider the
11 Navier-Cauchy equation which characterizes small elastic deformations and serves, for instance, as
12 a model for respiratory motion. Our goal is to provide a proof-of-concept that by incorporating
13 the deformation fields provided by this PDE, one can reduce the respective motion artefacts in
14 the reconstructed image. To this end, we solve the Navier-Cauchy equation prior to the image
15 reconstruction step using suitable initial and boundary data. Then, the thus computed deformation
16 fields are incorporated into an analytic dynamic reconstruction method to compute an image of the
17 unknown interior structure. The feasibility is illustrated with numerical examples from computerized
18 tomography.

19 **Key words.** Dynamic inverse problems, Tomography, Motion estimation, Elasticity equation

20 **AMS subject classifications.** 44A12, 65R32, 92C55, 74B05

21 **1. Introduction.** Imaging modalities are concerned with the non-invasive recovery
22 of some characteristic function of an object under investigation from measured
23 data. Hence, they represent a well-known application of the theory of inverse problems
24 which are concerned with determining the cause of an observation. If the specimen is
25 stationary during the data collection, the reconstruction process is well understood for
26 most imaging systems [36]. A dynamic behaviour of the object during measurement,
27 however, results in inconsistent data, and standard reconstruction techniques derived
28 under the stationary assumption lead to severe motion artefacts in the computed
29 images [13, 31, 42]. This affects medical applications, for instance due to respiratory
30 and cardiac motion, as well as non-destructive testing while imaging driven liquid
31 fronts for oil recovery studies [3] or while performing elasticity experiments during
32 the scan to determine material parameters [25].

33 Solving the dynamic reconstruction problem requires to model and incorporate
34 dynamical prior information within the reconstruction step. For individual imaging
35 modalities like computerized tomography, magnetic resonance imaging or positron
36 emission tomography, several methods of this type have been proposed in the litera-
37 ture, based on rebinning or gating the data [15, 33, 46], a variational formulation [6, 14,
38 32, 37], exact analytic methods [11, 12, 16], iterative procedures [2, 24] or approximate
39 inversion formulas [18, 26, 27]. Further, regularization techniques developed in the
40 general context of dynamic linear inverse problems [9, 17, 29, 40, 41] have been success-
41 fully applied to imaging problems.

*Submitted to the editors DATE.

Funding: The work of the first and second author was supported by the Deutsche Forschungsgemeinschaft under grant HA 8176/1-1.

[†]Department of Mathematics, University of Stuttgart (bernadette.hahn@imng.uni-stuttgart.de, melina-loren.kienle-garrido@imng.uni-stuttgart.de).

[‡]Department of Mathematics, University of Würzburg (klingen@mathematik.uni-wuerzburg.de, sandra.warnecke@mathematik.uni-wuerzburg.de).

42 The most efficient way to compensate for the dynamics is to model and incorporate
43 the motion prior in form of a deformation map Φ which describes the trajectory of the
44 particles in the interior of the object over time. In general, such deformation fields
45 are a priori unknown and have to be extracted from the measured data. Typically,
46 parametrized motion models are employed, i.e. only a few unknown parameters need
47 to be estimated, either via additional measurements [2, 11, 34, 39] or directly from the
48 recorded tomographic data. In computerized tomography, for instance, they can be
49 determined by detecting traces of nodal points in the sinogram [18, 33]. For global
50 rotations and translations, an estimation procedure using data consistency conditions
51 is proposed in [48]. Iterative procedures are, for example, based on edge entropy [28],
52 or perform estimation and reconstruction step simultaneously [45].

53 Alternatively, the dynamics can be characterized in terms of velocity fields be-
54 tween consecutive image frames. The intensity variations in the image sequence are
55 then linked to the underlying velocity field by the optical flow constraint, based on the
56 brightness constancy assumption. Recovering both velocity fields and image frames
57 from the measured data simultaneously requires solving non-convex optimization
58 problems of extremely large size [4, 5].

59 In this article, we pursue another approach. Many dynamic processes can be
60 described by partial differential equations, and thus, their (numerical) solution could
61 provide the required deformation fields. More precisely, we consider in the following
62 the Navier-Cauchy equation, representing linear elasticity. In applications in radio-
63 therapy treatment planning, the respective conservation laws are employed to model
64 respiratory motion [47].

65 To reduce the overall complexity and to provide a proof-of-concept that such
66 motion prior can compensate for the dynamics, we decouple both tasks for the study
67 in this article.

68 In Section 2, we recall the mathematical model of dynamic imaging and present
69 the general motion compensation strategy from [19] in the mass preserving case which
70 assumes that the motion is known. We then derive our elastic motion model based on
71 conservation laws in Section 3. The respective model in particular requires prescribed
72 initial and boundary data. Therefore, we discuss suitable choices which are feasible
73 regarding practical applications. The numerical calculation of the deformation fields
74 is studied in Section 4. Finally, the potential of the motion model for the purpose
75 of motion compensation is illustrated in Section 5 at the example of computerized
76 tomography, combining the numerically computed deformation fields with our dynam-
77 ic reconstruction strategy.

78 **2. Models and reconstruction strategies in dynamic imaging.** In this
79 section, we introduce the mathematical framework to formulate and address the
80 problem of dynamic image reconstruction. In particular, we will consider the two-
81 dimensional case throughout the article. Further, since the motion estimation ap-
82 proach via the Navier-Cauchy equation is not restricted to a particular imaging
83 modality, we want to present the motion compensation strategy in a framework
84 covering many different modalities. A detailed introduction can be found for instance
85 in [17, 19].

86 We start by deriving the model of the stationary setting. To be more intuitive,
87 we first consider the example of computerized tomography (CT). In CT, X-ray beams
88 are transmitted through the specimen of interest to a detector where the intensity loss
89 of the X-rays is recorded. In particular, the radiation source needs to rotate around
90 the object to capture information from different angles of view. Due to this rotation,

91 the data acquisition takes a considerable amount of time. The mathematical model
 92 for this imaging process is given by the Radon transform

$$93 \quad (2.1) \quad \mathcal{R}h(t, y) = \int_{\mathbb{R}^2} h(x) \delta(y - x^T \theta(t)) dx, \quad (t, y) \in [0, 2\pi] \times \mathbb{R},$$

which integrates h along the straight lines $\{x \in \mathbb{R}^2 : x^T \theta(t) = y\}$, i.e. along the path of the emitted X-rays. In particular, the unit vector $\theta(t) = (\cos(t), \sin(t))^T$ characterizes the source position at time instance t , while y denotes the affected detector point, and δ stands for the delta distribution. The goal is then to recover h , the linear attenuation coefficient of the studied specimen, from measurements $g(t, y) = \mathcal{R}h(t, y)$ with $(t, y) \in [0, 2\pi] \times \mathbb{R}$. Using the Fourier transform of δ , we further obtain the equivalent representation

$$\mathcal{R}h(t, y) = \int_{\mathbb{R}} \int_{\mathbb{R}^2} (2\pi)^{-1/2} e^{i\sigma(y - x^T \theta(t))} h(x) dx d\sigma.$$

94 Besides CT, many imaging modalities in the stationary setting can be modeled
 95 mathematically by a linear operator which integrates the searched-for quantity along
 96 certain manifolds, for instance along circles, respectively spheres, in SONAR or photo-
 97 acoustic tomography. Thus, we consider in the following a more general framework,
 98 namely model operators of type

$$99 \quad (2.2) \quad \mathcal{A}h(t, y) = \int_{\mathbb{R}} \int_{\Omega_x} h(x) a(t, y, x) e^{i\sigma(y - H(t, x))} dx d\sigma, \quad (t, y) \in \mathbb{R}_T \times \Omega_y,$$

100

101 where Ω_x and Ω_y denote open subsets of \mathbb{R}^2 and \mathbb{R} , respectively, $\mathbb{R}_T \subset \mathbb{R}$ represents
 102 an open time interval covering the time required for the measuring process, $a \in$
 103 $C^\infty(\mathbb{R}_T \times \Omega_y \times \Omega_x)$ is a weight function and $H : \mathbb{R}_T \times \mathbb{R}^2 \rightarrow \mathbb{R}$ characterizes the
 104 manifold we are integrating over.

105 With this observation model, we can formulate the associated inverse problem:
 106 Determine h from measured data

$$107 \quad (2.3) \quad g(t, y) = \mathcal{A}h(t, y), \quad (t, y) \in \mathbb{R}_T \times \Omega_y.$$

109 The component t of the data variable expresses the time-dependency of the data
 110 collection process. The searched-for quantity h itself, however, is independent of
 111 time, i.e. (2.3) corresponds to a *static* image reconstruction problem. We refer to
 112 equation (2.3) also as *static inverse problem*.

113 **2.1. The mathematical model of dynamic imaging.** Now, we consider the
 114 dynamic case, i.e. the investigated object changes during collection of the data and
 115 is therefore characterized by a time-dependent function $f : \mathbb{R}_T \times \mathbb{R}^2 \rightarrow \mathbb{R}$. For a fixed
 116 time, we abbreviate $f_t := f(t, \cdot)$, i.e. f_t represents the state of the object at time
 117 instance t . Then, the inverse problem of the dynamic scenario reads

$$118 \quad (2.4) \quad \mathcal{A}^{dyn} f(t, y) = g(t, y)$$

120 with the dynamic operator $\mathcal{A}^{dyn} f(t, y) := \mathcal{A}f_t(t, y)$. In particular, only measurements
 121 $g(t, \cdot)$ for a single time instance encode information about the state f_t , which is
 122 typically not sufficient to fully recover f_t . In CT, only line integrals in one particular
 123 direction would be available for the reconstruction of f_t , which is well known to be

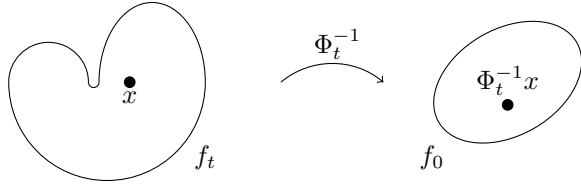


Figure 1: The mapping Φ_t^{-1} correlates the state f_t at time t to the reference state f_0 at the initial time.

124 insufficient. Thus, additional information about the dynamic behavior need to be
 125 incorporated in order to solve dynamic inverse problems.

126 The dynamic behaviour of the object can be considered to be due to particles
 127 which change position in a fixed coordinate system of \mathbb{R}^2 . This physical interpretation
 128 of object movement can then be incorporated into a mathematical model $\Phi : \mathbb{R}_T \times$
 129 $\mathbb{R}^2 \rightarrow \mathbb{R}^2$, where $\Phi(0, x) = x$, i.e. we consider f_0 as reference state, and $\Phi(t, x)$
 130 denotes the position at time t of the particle initially at x . For fixed $t \in \mathbb{R}_T$, we write
 131 $\Phi_t x := \Phi(t, x)$ to simplify the notation. Motivated by medical applications, where no
 132 particle is lost or added and two particles cannot move to the same position at the
 133 same time, Φ_t is assumed to be a diffeomorphism for all $t \in \mathbb{R}_T$. Thus, a particle
 134 $x \in \mathbb{R}^2$ at time t is at position $\Phi_t^{-1}x$ in the reference state, see Figure 1. A description
 135 of this motion model can also be found, for instance, in [17, 26, 27].

136 Using this motion model and the initial state function f_0 , we find the state of the
 137 object at time instance t to be

138 (2.5)
$$f(t, x) = f_0(\Phi_t^{-1}x) |\det D\Phi_t^{-1}x|$$

140 by taking into account that the mass shall be preserved.

141

142 Inserting the property (2.5) in the definition of the dynamic forward operator
 143 \mathcal{A}^{dyn} , we obtain an operator \mathcal{A}_Φ for the initial state function, namely

144 (2.6)
$$\mathcal{A}_\Phi f_0(t, y) := \mathcal{A}(|\det D\Phi_t^{-1}(\cdot)| (f_0 \circ \Phi_t^{-1}))(t, y).$$

146 *Remark 2.1.* In our previous work [17, 18, 21], we considered the intensity preserv-
 147 ing model

148
$$f(t, x) = f_0(\Phi_t^{-1}x),$$

149 i.e. each particle keeps its initial intensity over time. Although this does not alter
 150 the nature of our reconstruction algorithm, we insist here on the mass preserving case
 151 to be consistent with the conservation laws employed in Section 3 for the purpose
 152 of motion estimation and clinical applications. The mass preserving model is also
 153 considered, for instance, in [26, 27].

154 For a theoretical analysis, the motion model Φ is typically assumed to satisfy the
 155 following additional conditions, cf. [8, 20, 21, 38]:

- 156 • The map

157 (2.7)
$$x \mapsto \begin{pmatrix} H(t, \Phi_t x) \\ D_t H(t, \Phi_t x) \end{pmatrix}$$

158 is one-to-one for each t .

159 • It holds

$$160 \quad (2.8) \quad \det \begin{pmatrix} D_x H(t, \Phi_t x) \\ D_x D_t H(t, \Phi_t x) \end{pmatrix} \neq 0$$

161 for all $x \in \mathbb{R}^2$ and all $t \in \mathbb{R}_T$.

162 Basically, these properties ensure that the object's motion does not result in trivial
163 sampling schemes for f_0 . A detailed interpretation of these conditions can be found,
164 for instance, in [21].

165 If the deformation fields Φ_t are known, the dynamic inverse problem (2.4) reduces
166 to determining f_0 from the equation

$$167 \quad (2.9) \quad \mathcal{A}_\Phi f_0 = g.$$

169 In [17, 19, 26], efficient algorithms have been developed to solve this task. The
170 underlying strategy proposed in [19] is summarized in the following, before we intro-
171 duce our PDE-based approach to determine the deformation fields Φ_t in Section 3
172 and combine both strategies to solve (2.9) when Φ_t are unknown.

173 **2.2. Motion compensation algorithms.** Throughout this section, we assume
174 the motion Φ to be known and focus on solving (2.9). Under suitable assumptions on
175 the phase function H , the linear integral operator \mathcal{A} from the underlying static case
176 belongs to the class of *Fourier integral operators*. To define this type of operators, we
177 first introduce the concepts of amplitude and phase function.

178 DEFINITION 2.2.

180 • Let $\Lambda \in C^\infty(\mathbb{R}_T \times \Omega_y \times \Omega_x \times \mathbb{R} \setminus \{0\})$ be a real-valued function with the following
181 properties:

- 182 1. Λ is positive homogeneous of degree 1 in σ , i.e. $\Lambda(t, y, x, r\sigma) =$
183 $r\Lambda(t, y, x, \sigma)$ for every $r > 0$,
- 184 2. both $(\partial_{(t,y)}\Lambda, \partial_\sigma\Lambda)$ and $(\partial_x\Lambda, \partial_\sigma\Lambda)$ do not vanish for all $(t, y, x, \sigma) \in$
185 $\mathbb{R}_T \times \Omega_y \times \Omega_x \times \mathbb{R} \setminus \{0\}$,
- 186 3. it holds $\partial_{(t,y,x)} \left(\frac{\partial\Lambda}{\partial\sigma} \right) \neq 0$ on the zero set

$$187 \quad \Sigma_\Lambda = \{(t, y, x, \sigma) \in \mathbb{R}_T \times \Omega_y \times \Omega_x \times \mathbb{R} \setminus \{0\} : \partial_\sigma\Lambda = 0\}.$$

189 Then, Λ is called a non-degenerate phase function.

190 • Let $a \in C^\infty(\mathbb{R}_T \times \Omega_y \times \Omega_x \times \mathbb{R})$ satisfy the following property:
191 For every compact set $K \subset \mathbb{R}_T \times \Omega_y \times \Omega_x$ and for every $M \in \mathbb{N}$, there exists
192 a $C = C(K, M) \in \mathbb{R}$ such that

$$193 \quad \left| \frac{\partial^{n_1}}{\partial t^{n_1}} \frac{\partial^{n_2}}{\partial y^{n_2}} \frac{\partial^{n_3}}{\partial x_1^{n_3}} \frac{\partial^{n_4}}{\partial x_2^{n_4}} \frac{\partial^m}{\partial \sigma^m} a(t, y, x, \sigma) \right| \leq C(1 + |\sigma|)^{k-m}$$

195 for $n_1 + n_2 + n_3 + n_4 \leq M$, $m \leq M$, for all $(t, y, x) \in K$ and for all $\sigma \in \mathbb{R}$.

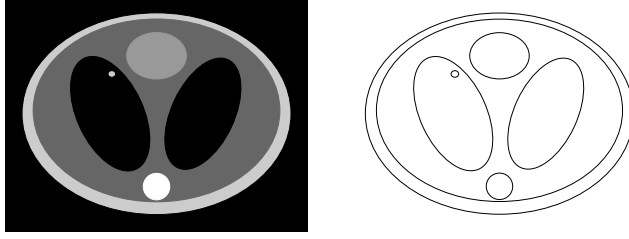
196 Then a is called an amplitude (of order k).

197 • Let Λ denote a non-degenerate phase function and let a be an amplitude (of
198 order k). Then, the operator \mathcal{T} defined by

$$199 \quad \mathcal{T}u(t, y) = \int u(x) a(t, y, x, \sigma) e^{i\Lambda(t, y, x, \sigma)} dx d\sigma, \quad (t, y) \in \mathbb{R}_T \times \Omega_y$$

200

201 is called a Fourier integral operator (FIO) (of order $k - 1/2$).

Figure 2: Initial state f_0 of a phantom (left) and its singularities (right).

202 For more details and a more general definition see [22, 44].

203

204 In [19, 20], it was shown that under suitable smoothness conditions on Φ , the
205 dynamic operator \mathcal{A}_Φ inherits the FIO property from its static counterpart \mathcal{A} .

206 **THEOREM 2.3.** *Let $\Phi \in C^\infty(\mathbb{R}_T \times \mathbb{R}^2)$ and let Φ_t be a diffeomorphism for every
207 $t \in \mathbb{R}_T$. If the static operator \mathcal{A} from (2.2) is an FIO, the respective dynamic operator
208 \mathcal{A}_Φ from (2.6) is an FIO as well.*

209 Fourier integral operators have specific properties that can be used to design
210 efficient motion compensation strategies: They encode characteristic features of the
211 object - the so-called *singularities* - in precise and well-understood ways.

212 Formally, singularities of a (generalized) function h correspond to the elements
213 of the *singular support* $\text{ssupp}(h)$, which denotes the complement of the largest open
214 set on which h is smooth. In imaging applications, where the searched-for quantity
215 is typically piecewise constant (each value characterizing a particular material), the
216 singularities correspond to the contours of h , see Figure 2.

217 The method for motion compensation from [19] is motivated by results on micro-
218 local analysis, which address - among others - the question which singularities can be
219 stably recovered from the data. The main idea is to use reconstruction operators of
220 the form

$$221 \quad (2.10) \quad \mathcal{L}_\Phi = \mathcal{B}_\Phi \mathcal{P}$$

223 on the data $g = \mathcal{A}_\Phi f_0$ with \mathcal{P} a *pseudodifferential operator* (typically acting on the
224 spatial data variable y) and a *backprojection operator* \mathcal{B}_Φ which incorporates the
225 information on the dynamic behavior.

DEFINITION 2.4. a) *An operator of the form*

$$\mathcal{P}g(t, s) = \int_{\mathbb{R}} \int_{\mathbb{R}} e^{i\sigma(s-y)} p(s, y, \sigma) g(t, y) dy d\sigma$$

226 *with $|\sigma| \leq 1$ and amplitude p which is locally integrable for s, y in any compact
227 set K is called pseudodifferential operator (PSIDO) (acting on the spatial
228 data variable y).*

229 b) *The operator*

$$230 \quad \mathcal{B}_\Phi g(x) = \int_{\mathbb{R}_T} b(t, x) g(t, H(t, \Phi_t x)) dt, \quad x \in \mathbb{R}^2,$$

231
232 *where $b(t, x)$ is a positive C^∞ -weight function on $\mathbb{R}_T \times \mathbb{R}^2$, is called backpro-
233 jection operator associated to \mathcal{A}_Φ .*

234 With these representations of \mathcal{B}_Φ and \mathcal{P} , the operator \mathcal{L}_Φ from (2.10) reads

$$235 \quad (2.11) \quad \mathcal{L}_\Phi g(x) = \int_{\mathbb{R}_T} \int_{\mathbb{R}} \int_{\mathbb{R}} b(t, x) p(H(t, \Phi_t x), y, \sigma) g(t, y) e^{i\sigma(H(t, \Phi_t x) - y)} dy d\sigma dt.$$

236 *Remark 2.5.* a) Pseudodifferential operators constitute a special case of an
 237 FIO. A more general definition than the one given above can be found, for
 238 instance, in [30].

239 b) If we choose the weight $b(t, x) = a(t, H(t, \Phi_t), \Phi_t x)$ with the amplitude a of
 240 the underlying static operator \mathcal{A} , the respective backprojection operator \mathcal{B}_Φ
 241 corresponds to the dual operator of \mathcal{A}_Φ .

242 The following result forms the basis to our motion compensation method.

243 **THEOREM 2.6.** *Let $\Phi \in C^\infty(\mathbb{R}_T \times \mathbb{R}^2)$ and let $\Phi_t, t \in \mathbb{R}_T$ be diffeomorphisms that*
 244 *satisfy the conditions (2.7) and (2.8). Further, let $\mathcal{L}_\Phi = \mathcal{B}_\Phi \mathcal{P}$ be well-defined. Then,*
 245 *\mathcal{L}_Φ preserves the contours of f_0 which are ascertained in the measured data.*

246 *Proof.* The statement follows directly from Theorem 13 in [20]. \square

247 **Interpretation:** Applying a reconstruction operator \mathcal{L}_Φ of type (2.10) provides
 248 an image showing the singularities of f_0 correctly, which are encoded by the dynamic
 249 data. In particular, no motion artefacts arise. Thus, the described approach provides
 250 in fact a motion compensation strategy. In particular, it can be easily implemented
 251 and the computational effort is comparable to the one of static reconstruction algo-
 252 rithms of type *filtered backprojection*. If an inversion formula of type $u = \mathcal{A}^* \mathcal{P}^{stat} \mathcal{A} u$
 253 with a PSIDO \mathcal{P}^{stat} is known for the static case, then choosing the PSIDO $\mathcal{P} = \mathcal{P}^{stat}$
 254 for the motion compensation strategy provides even a good approximation to the exact
 255 density values of f_0 [19]. In computerized tomography, such an inversion formula is
 256 known with \mathcal{P}^{stat} being the *Riesz potential* [35].

257
 258 *Remark 2.7.* Although the ascertained singularities of f_0 are correctly recon-
 259 structed by \mathcal{L}_Φ , some additional artefacts might occur if the motion is non-periodic.
 260 This has been studied in detail for computerized tomography in [21] and for a more
 261 general class of imaging problems in [20]. These artefacts would be caused by singular-
 262 ities encoded at beginning and end of the scanning and would spread along the
 263 respective integration curve. Nevertheless, this is an intrinsic property due to the
 264 nature of the dynamic problem and therefore does not impose a major restriction
 265 to our reconstruction approach. In particular, for periodic motion as in medical
 266 applications, such as respiratory or cardiac motion, the data acquisition protocol
 267 could be adjusted to the breathing or cardiac cycle to avoid this issue.

268 Since inverse problems are typically ill-posed, a regularization is required to
 269 determine $\mathcal{L}_\Phi g$ stably from the measured data $g = \mathcal{A}_\Phi f_0$. For our considered class
 270 of imaging problems, the ill-posedness is typically revealed by the growth of the
 271 symbol p in terms of σ . For instance, the amplitude of the Riesz potential arising in
 272 computerized tomography corresponds to $p(s, y, \sigma) = p(\sigma) = |\sigma|$, thus, amplifying the
 273 high frequencies of the data g . The inversion process can be stabilized by introducing
 274 a smooth low-pass filter e^γ , i.e. by considering

$$275 \quad (2.12) \quad \mathcal{L}_\Phi^\gamma g(x) = \int_{\mathbb{R}_T} \int_{\mathbb{R}} \int_{\mathbb{R}} b(t, x) p(H(t, \Phi_t x), y, \sigma) e^\gamma(\sigma) g(t, y) e^{i\sigma(H(t, \Phi_t x) - y)} dy d\sigma dt$$

276 with $\gamma > 0$ instead of (2.11), see [19] for more details.

277 **2.3. Reconstruction operator in dynamic CT.** Since we will evaluate our
 278 motion estimation strategy in Section 5 at the example of computerized tomography,
 279 we want to state the respective motion compensation algorithm for this application
 280 explicitly.

As introduced in the beginning of this section, the mathematical model operator \mathcal{A} of the static case corresponds to the classical Radon transform \mathcal{R} , see (2.1), which is an FIO with amplitude $a(t, y, x) = (2\pi)^{-1/2}$ and phase function $\Lambda(t, y, x, \sigma) = \sigma(y - H(t, x))$, where $H(t, x) = x^T \theta(t)$ [30]. Thus, the associated dynamic backprojection operator \mathcal{B}_Φ with weight $b(t, x) = a(t, H(t, \Phi_t), \Phi_t x) = (2\pi)^{-1/2}$ reads

$$\mathcal{B}_\Phi g(x) = (2\pi)^{-1/2} \int_{\mathbb{R}_T} g(t, (\Phi_t x)^T \theta(t)) dt.$$

281 Choosing as PSIDO the Riesz potential with amplitude $p(s, y, \sigma) = |\sigma|$ and a low-pass
 282 filter e^γ , for instance the Gaussian, we obtain the dynamic reconstruction operator

283
$$\mathcal{L}_\Phi^\gamma g(x) = (2\pi)^{-1/2} \int_{\mathbb{R}_T} \int_{\mathbb{R}} \int_{\mathbb{R}} |\sigma| e^\gamma(\sigma) g(t, y) e^{i\sigma((\Phi_t x)^T \theta(t) - y)} dy d\sigma dt, \quad \gamma > 0,$$

284 which can be implemented in form of a *filtered backprojection* type algorithm, see [18].

285 **3. Linear elastics.** In this section and the following one, we will treat the task
 286 of motion estimation. While, for a global deformation, the dynamic behavior of
 287 the boundary can be observed externally, the deformation in the interior is a priori
 288 unknown. Since many dynamic processes can be mathematically described in terms
 289 of a partial differential equation (PDE), we propose to determine the deformation
 290 fields Φ_t by finding the solution of an appropriate PDE with suitable given initial and
 291 boundary data.

292 Since the deformation fields $\Phi_t, t \in \mathbb{R}_T$ describe the mapping from the initial/reference
 293 state to the current position, we choose the Lagrangian description for the PDE. Let
 294 $\Omega_x \subset \mathbb{R}^2$ denote the initial domain, i.e. Ω_x corresponds to the support of the initial
 295 state f_0 , and consequently, we choose Ω_x to be the reference configuration.

297 We require that $\Phi_t, t \in \mathbb{R}_T$ preserves its orientation meaning that $\det D\Phi(t, x) > 0$
 298 for all $(t, x) \in \mathbb{R}_T \times \Omega_x$. Especially in medical applications, this assumption is sensible
 299 since it also states that the local ratio of the current and the initial volume never
 300 vanishes. [1]

302 The following definition links the current and the initial position.

303 **DEFINITION 3.1.** *The difference between the current and the initial position is*
 304 *called displacement $u(t, x) = \Phi(t, x) - x$ for all $(t, x) \in \mathbb{R}_T \times \Omega_x$.*

305 We are driven by medical applications. Respiratory or cardiac motion, for in-
 306 stance, have properties which shall be reflected by adequate equations. Due to their
 307 periodic behavior, it is clear that occurring stresses do not cause any yielding. So
 308 we assume a linear relationship between stresses and strain which results in linear
 309 elasticity.

310 Inserting Hooke's law in the general equation of conservation of momentum, we
 311 come to the Navier-Cauchy equations in two spatial dimensions for $(t, x) \in \mathbb{R}_T \times \Omega_x$,

312 see for reference [43]:

(3.1)

$$313 \quad \hat{\rho} \frac{\partial^2 u_k}{\partial t^2} = \hat{v}_k + \mu \left(\frac{\partial^2 u_k}{\partial x_1^2} + \frac{\partial^2 u_k}{\partial x_2^2} \right) + (\lambda + \mu) \frac{\partial}{\partial x_k} \left(\frac{\partial u_1}{\partial x_1} + \frac{\partial u_2}{\partial x_2} \right) \quad \text{for } k = 1, 2.$$

315 These are two linear PDEs for the two unknown components u_1, u_2 of the displace-
316 ment u with the following parameters:

- 317 • The density $\hat{\rho} = \rho(t, x) \det D\Phi(t, x)$ equals the initial density distribution
- 318 $\hat{\rho} = \hat{\rho}(x) = \rho(0, x)$ due to the conservation of mass.
- 319 • The external volume forces are denoted by $\hat{v} = v(t, x) \det D\Phi(t, x)$, where
- 320 $v : \mathbb{R}_T \times \Omega_x \rightarrow \mathbb{R}^2$ describes the volume force density.
- 321 • The Lamé-coefficients λ and μ specify the behavior of the material.

322 For a fully determined problem, we need the displacements at time $t = 0$ and
323 their time derivatives as initial data

$$324 \quad u(0, x) = \vartheta^0(x) \quad \text{and} \quad \frac{\partial}{\partial t} u(0, x) = \vartheta^1(x),$$

326 with some given $\vartheta^0, \vartheta^1 : \Omega_x \rightarrow \mathbb{R}^2$.

327 Also the behavior of the boundary needs to be known, more precisely a function
328 $\psi : \mathbb{R}_T \times \Omega_x \rightarrow \mathbb{R}^2$ prescribing the evolution of the displacements on the boundary of
329 the domain $\Gamma = \partial\Omega_x$:
330

$$331 \quad u(t, x) = \psi(t, x) \quad \text{for } (t, x) \in \mathbb{R}_T \times \Gamma.$$

333 Solving the introduced PDE with given initial and boundary conditions corre-
334 sponds to determining the displacement u , respectively the deformation Φ in the
335 interior of the object from observations of the dynamic behavior of the object's
336 boundary. Thus, it provides exactly the information about the motion needed for
337 our motion compensation algorithm.
338

339 Under some regularity assumptions, existence and uniqueness of the solutions of
340 the Navier-Cauchy equation (3.1) can be proven. If the initial data is C^∞ , solutions
341 for the initial value problem stay C^∞ , cf. [23]. Also for the initial-boundary value
342 problem, there are existence and uniqueness results, cf. [7]. For appropriate boundary
343 data ψ , regularity of the solutions does not get lost, and it can be shown that the
344 solutions are diffeomorphisms, cf. [10]. In our numerical experiments in Section 5, the
345 initial and boundary data is chosen so that the application of the motion compensation
346 algorithm goes through.
347

348 In the following, we quickly discuss suitable initial and boundary data regarding
349 our application in dynamic imaging. As mentioned before, a global motion can be
350 observed externally, thus, we make the reasonable assumption that the boundary data
351 $\psi(t, x)$, $(t, x) \in \mathbb{R}_T \times \Gamma$ are given. However, in practice, only discrete boundary data
352 $\psi(t_n, x_{i,j})$, $n = 1, \dots, N$, $i = 1, \dots, I$, $j = 1, \dots, J$, $N, I, J \in \mathbb{N}$ will be available which
353 might be even sparse with respect to the spatial component (i.e. I, J might be small)
354 or corrupted by noise. This will be addressed in our numerical study in Section 5.

355 Since we are overall interested in a reconstruction of the initial state of the
356 object and since the underlying motion model considers small deformations, the initial
357 displacement data ϑ^0 and ϑ^1 will be set to zero.

358 *Remark 3.2.* According to (3.1), the Navier-Cauchy contains the initial density
 359 distribution $\hat{\rho}$ as parameter which is strongly linked to the quantity f_0 we would like to
 360 determine by our imaging modality (in particular, they share the same singularities).
 361 If we knew this parameter $\hat{\rho}$, we would already have full knowledge about the interior
 362 structure of the studied specimen. Thus, we cannot assume to know $\hat{\rho}$. Formally, we
 363 could formulate a joint motion estimation and image reconstruction approach, where
 364 we identify the parameter $\hat{\rho}$ of the PDE using the measurements from our imaging
 365 modality. However, to simplify the task for our proof-of-concept study, we propose
 366 another approach. In order to decouple the tasks of motion estimation via the Navier-
 367 Cauchy equation and dynamic image reconstruction, we use for the solution of the
 368 PDE a simplified prior instead of the exact density distribution $\hat{\rho}$. This is discussed
 369 in more detail in Section 5.

370 **4. Numerical solution of the Navier-Cauchy equation.** We divide the
 371 given time period $t \in \mathbb{R}_T$ into equidistant intervals and call the time steps $t_n = n \cdot \Delta t$.
 372 We choose a Cartesian grid (not necessarily uniform) so that the discrete boundary
 373 lies on the continuous boundary, see Figure 4. Using central finite differences of second
 374 order for the discretization of the Navier-Cauchy equation (3.1), we obtain an explicit
 375 numerical scheme.

376 We denote $x_{i,j} = ((x_1)_i, (x_2)_j) = (x_i, y_j)$, $(u_k)_{i,j}^n = u_k(t_n, x_{i,j})$ for $k = 1, 2$,
 377 $\rho_{i,j}^0 = \hat{\rho}(x_{i,j})$, $\hat{v}_{i,j}^n = \hat{v}(t_n, x_{i,j})$, $\Delta x_i = x_{i+1} - x_i$ and $\Delta y_j = y_{j+1} - y_j$. Then the
 378 scheme reads exemplary for the first component $k = 1$

$$\begin{aligned}
 379 \quad (u_1)_{i,j}^{n+1} &= \frac{\Delta t^2}{\rho_{i,j}^0} \hat{v}_{i,j}^n - (u_1)_{i,j}^{n-1} + 2 \left[1 - \frac{2\Delta t^2}{\rho_{i,j}^0} \left(\frac{\mu}{\Delta y_j^2 + \Delta y_{j-1}^2} + \frac{\lambda + 2\mu}{\Delta x_i^2 + \Delta x_{i-1}^2} \right) \right] (u_1)_{i,j}^n \\
 380 \quad &+ \frac{\Delta t^2}{\rho_{i,j}^0} \frac{2(\lambda + 2\mu)}{\Delta x_i^2 + \Delta x_{i-1}^2} \left[\left(1 - \frac{\Delta x_i - \Delta x_{i-1}}{\Delta x_i + \Delta x_{i-1}} \right) (u_1)_{i+1,j}^n + \left(1 + \frac{\Delta x_i - \Delta x_{i-1}}{\Delta x_i + \Delta x_{i-1}} \right) (u_1)_{i-1,j}^n \right] \\
 381 \quad &+ \frac{\Delta t^2}{\rho_{i,j}^0} \frac{2\mu}{\Delta y_j^2 + \Delta y_{j-1}^2} \left[\left(1 - \frac{\Delta y_j - \Delta y_{j-1}}{\Delta y_j + \Delta y_{j-1}} \right) (u_1)_{i,j+1}^n + \left(1 + \frac{\Delta y_j - \Delta y_{j-1}}{\Delta y_j + \Delta y_{j-1}} \right) (u_1)_{i,j-1}^n \right] \\
 382 \quad &+ \frac{\Delta t^2}{\rho_{i,j}^0} \frac{\lambda + \mu}{(\Delta x_i + \Delta x_{i-1})(\Delta y_j + \Delta y_{j-1})} \left((u_2)_{i+1,j+1}^n - (u_2)_{i-1,j+1}^n - (u_2)_{i+1,j-1}^n + (u_2)_{i-1,j-1}^n \right). \\
 383
 \end{aligned}$$

384 The corresponding stencil is illustrated in Figure 3.
 385 For the first time step, the (discrete) initial condition needs to be inserted

$$\begin{aligned}
 386 \quad (u_k)_{i,j}^{-1} &= (u_k)_{i,j}^1 - 2\Delta t \vartheta^1(x_{i,j}) \quad \text{for } k = 1, 2. \\
 387
 \end{aligned}$$

388 The stencil for the spatial discretization has nine nodes. Since we are inspired by
 389 medical applications and a thorax is a possible specimen to be studied, we might deal
 390 with curved domains. For curved domains at the boundary, for the update scheme
 391 there is a node, which is not available to the stencil, see Figure 4. Hence, we need to
 392 use an interpolation method.

393 For reasons of stability, we want to maintain the stencil. We call the missing node
 394 a ghost node that needs to have a value assigned to it, and we denote h the quantities
 395 given at every node. The indices of the nodes are given in Figure 4. A second-order
 396 approach is the following one for the components $k = 1, 2$:

$$\begin{aligned}
 397 \quad (h_k)_{\text{ghost}} &= (h_k)_0 + \frac{(h_k)_{\text{aux}} - (h_k)_0}{(x_k)_{\text{aux}} - (x_k)_0} ((x_k)_{\text{ghost}} - (x_k)_0) \\
 398
 \end{aligned}$$

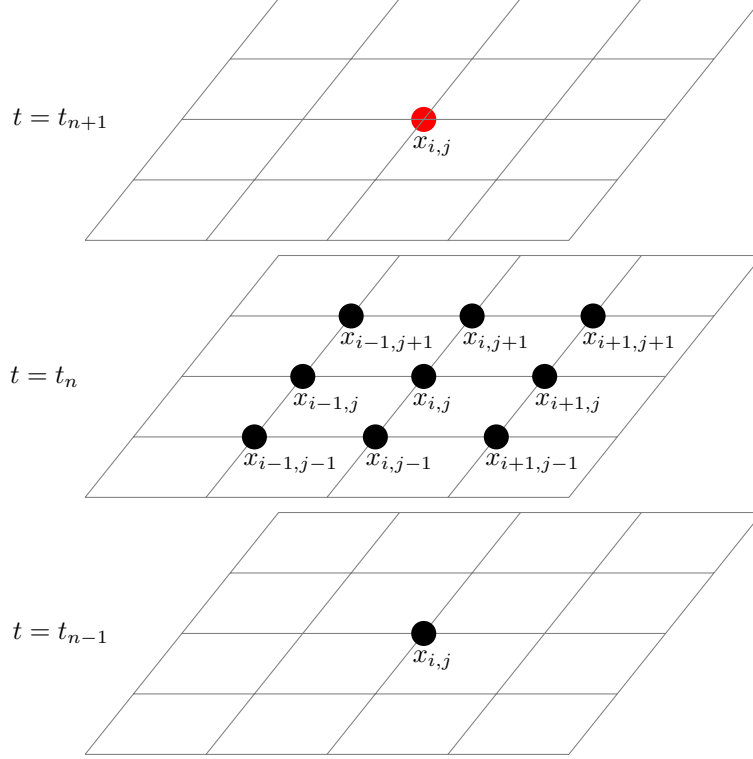


Figure 3: We illustrate the stencil for our numerical scheme. For the update of the values at node $x_{i,j}$ from $t_n \rightarrow t_{n+1}$, we have to provide information about the values at the other marked nodes.

399 where the auxiliary node on the continuous boundary is approximated by

$$400 \quad x_{\text{aux}} = \frac{1}{2} ((x_1)_1 + (x_1)_0), \quad y_{\text{aux}} = \frac{1}{2} ((x_2)_2 + (x_2)_0) \quad \text{and}$$

$$401 \quad (h_k)_{\text{aux}} = \frac{1}{2} ((h_k)_1 + (h_k)_2).$$

402 We use the CFL condition

$$404 \quad \frac{\nu_x \Delta t}{\Delta x} + \frac{\nu_y \Delta t}{\Delta y} \leq 1,$$

405 where $\Delta x := \min \Delta x_i$ and $\Delta y := \min \Delta y_j$, in order to determine a suitable time step Δt . The maximal propagation speeds are bounded from above by $\nu_x, \nu_y \leq \sqrt{(\lambda + 2\mu)/\rho}$ with $\rho := \min \rho_{i,j}^0 > 0$.

409 **5. Application in motion compensation.** We evaluate the motion estimation
 410 approach on simulated CT data. For this purpose, we consider a thorax phantom
 411 representing a cross-section of a chest, see Figure 5 left. Following from [11], its
 412 respiratory motion is modelled by an affine deformation, more precisely by

$$413 \quad \Phi(t, x) = \begin{pmatrix} s(t)^{-1} & 0 \\ 0 & s(t) \end{pmatrix} \left(x - \begin{pmatrix} 0.44 \cdot (s(t) - 1) \\ 0 \end{pmatrix} \right)$$

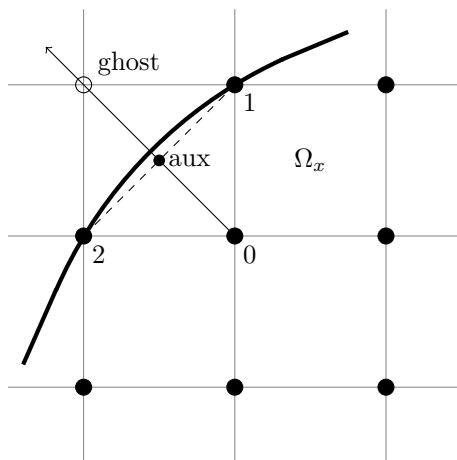


Figure 4: Illustration of the boundary: The nodes 1 and 2 lie directly on the continuous boundary, and their behaviour is prescribed by the Dirichlet data ψ . For the node 0, the stencil for the update scheme only can be applied with the help of an interpolation since the values of the ghost node are not available. The average of the values of the nodes 1 and 2 are used to create an auxiliary node which corresponds to a slightly ‘shifted’ boundary.

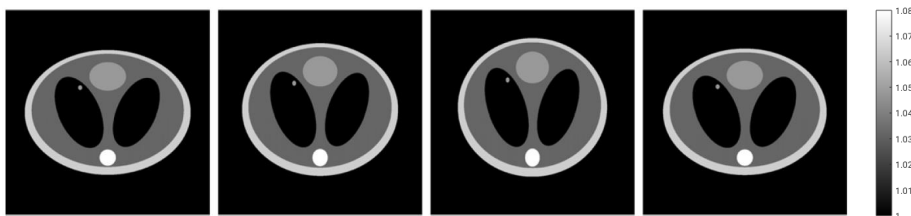


Figure 5: Cross-section of the numerical phantom during one cycling breath.

415 with $s(t) = 0.05 \cdot \cos(0.04 \cdot t) + 0.95$. The deformation during one breathing cycle is
 416 illustrated in the sequence of pictures in Figure 5.

417

418 The Radon data of this dynamic object are computed analytically for 660 source
 419 positions, uniformly distributed over the upper half sphere, and 451 discrete detector
 420 points uniformly distributed over $[-1, 1]$ (since the support of the phantom is con-
 421 tained in the unit disk at all time instances). Our reconstructions and - later on - all
 422 simulations of the PDE are run on a 257×257 grid.

423

424 If one does not take into account that the object was moving during data acquisi-
 425 tion and applies a static reconstruction algorithm to the dynamic data, an image of
 426 poor quality with motion artefacts such as blurring, streaking etc. is obtained, see
 427 Figure 6(b). This motivates the need for motion compensation and hence motion
 428 estimation strategies.

429

As motion compensation algorithm, we use the strategy specified in Section 2.3

430 with the Gaussian function as low-pass filter. The result of this algorithm with exact
 431 motion information Φ is shown in Figure 6(c). We observe that all components
 432 are indeed correctly reconstructed without motion artefacts, i.e. the motion is well
 433 compensated for, and in accordance to [19], we obtain a good approximation to
 434 the original initial state, cf. Figure 6(a). However, in practice, the exact motion
 435 information is typically unknown.

436 Thus, our goal is now to evaluate our proposed motion estimation strategy,
 437 i.e. the (discrete) deformation fields Φ_t are computed by solving the Navier-Cauchy
 438 equation with available initial and boundary data. First, we discuss the initial data
 439 corresponding to the initial density distribution $\hat{\rho}$. As discussed in Remark 3.2, this
 440 initial parameter is strongly linked to the searched-for initial state function f_0 which
 441 is why we propose to use a simplified prior instead. The one used for our simulation
 442 is shown in Figure 7. This prior only distinguishes between spine and soft tissue,
 443 where the respective values are initialized with standard values $\hat{\rho} = 1.85 \cdot 10^3 \text{ kg/m}^3$
 444 for the spine and $\hat{\rho} = 1.05 \cdot 10^3 \text{ kg/m}^3$ for the rest. This is indeed a reasonable prior
 445 in practice since the only component considered in the interior - the spine - typically
 446 does not move, so it can be extracted from a static reconstruction, cf. Figure 6(b).

447 Finding realistic values for the Lamé-coefficients is a research topic by itself. It
 448 is hard to quantify them and they differ depending on the study [47]. We assume a
 449 uniform motion behavior of all (soft) tissues and restrict ourselves to one set of values
 450 for the whole thorax. The coefficients are averaged to $\lambda = 3.46 \text{ kPa}$ and $\mu = 1.48 \text{ kPa}$.

451

452 Regarding the boundary data, we test several configurations. First, we use the
 453 exact analytical positions of the boundary. Then, solving the respective PDE as
 454 described in Section 4 and incorporating its solution as motion information in our
 455 dynamic reconstruction algorithm provides the reconstruction result shown in Figure
 456 6(d). The motion of the phantom is well compensated for and the small tumour is
 457 clearly visible. This shows that determining deformation fields by solving the Navier-
 458 Cauchy equation constitutes a valuable motion estimation strategy.

459 In practice, the boundary positions might be determined by attaching markers at
 460 the surface of the object. If these positions are determined by measurements, they will
 461 be subject to small measurement errors. Thus, in order to test stability with respect
 462 to the boundary data, we next add a sample of noise to the (analytical) boundary
 463 positions. The noise is generated as normal distribution around 0 with standard
 464 deviation 0.1 and 0.25, respectively. In Figure 8 we see that the reconstruction near
 465 the boundary is affected. More precisely, due to the inexact boundary positions, the
 466 boundary in the reconstruction appears fuzzy. However, the motion in the interior of
 467 the phantom is still well compensated for. All interior components, which correspond
 468 to the relevant searched-for information, including the small tumour, are still clearly
 469 recognizable, in particular in comparison to the static reconstruction, cf. Figure 6(b).

470 Further, we test the performance of the method if only a few discrete boundary
 471 positions are given. The motivation behind this experiment is that, in practice, only
 472 a limited number of marks can be attached to the surface of the object. To this
 473 end, we prescribe only 32 (and 16, respectively) grid nodes on the boundary. Between
 474 these nodes, we apply a linear interpolation. The results are displayed in Figure 9. We
 475 obtain some artefacts since the round shape of the thorax is replaced by a polygon due
 476 to the interpolation. However, as in the case of noisy boundary data, the deformation
 477 fields obtained by solving the PDE still provide sufficient information on the motion
 478 to compensate for it in the interior and to provide an image showing clearly all inner
 479 components including the small tumour.

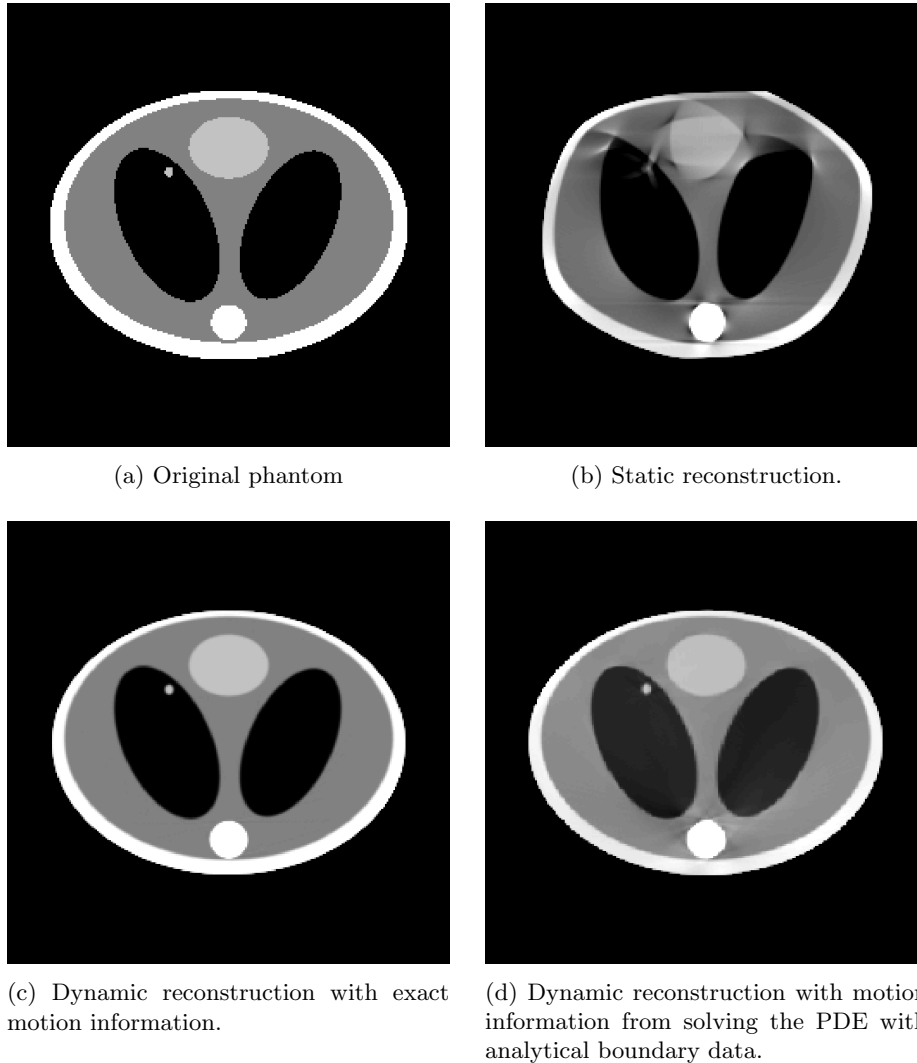


Figure 6: Static and dynamic reconstruction results of the initial state function.

480 **6. Conclusions.** This article provides a proof-of-concept for a motion estimation
 481 strategy in dynamic imaging, where the Navier-Cauchy equation serves as a mathe-
 482 matical model for small elastic deformations. To this end, we decoupled the tasks of
 483 motion estimation and image reconstruction, i.e. the Navier-Cauchy equation is solved
 484 prior to the reconstruction step using suitable and realistic initial and boundary data.
 485 Then the calculated deformation fields are incorporated into an analytic dynamic
 486 reconstruction algorithm. Our numerical results on a thorax phantom undergoing
 487 respiratory motion illustrate that this approach can significantly reduce motion arte-
 488 facts in the respective images. In particular, we discussed available boundary data
 489 and illustrated their affect on the reconstruction result.

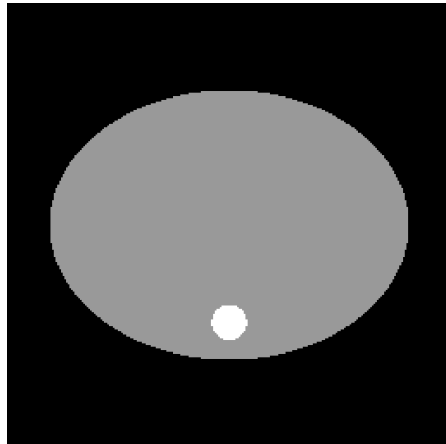
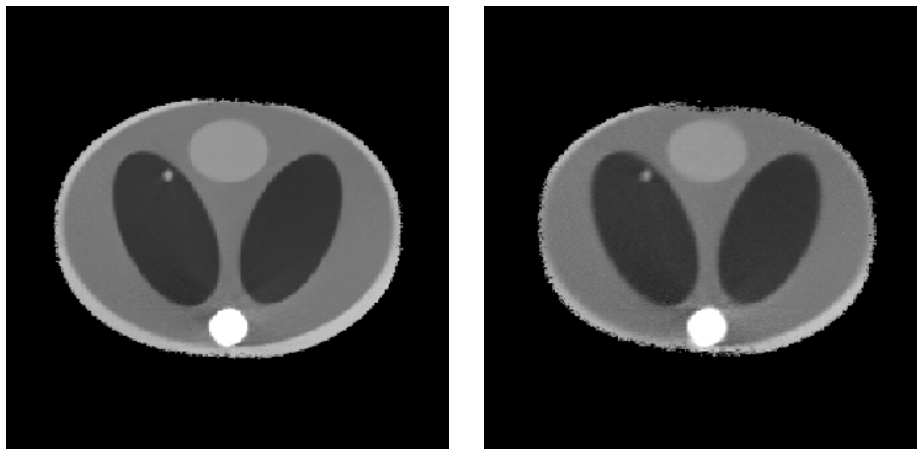


Figure 7: Initial density distribution used for solving the Navier-Cauchy equation.



(a) Result for noisy boundary data with standard deviation 0.1. (b) Result for noisy boundary data with standard deviation 0.25.

Figure 8: Dynamic reconstruction with motion information from solving the PDE with noisy boundary data.

490 **Acknowledgments.** The third and fourth author want to thank Matteo
 491 Semplice for fruitful discussions.

492 REFERENCES

493 [1] S. S. ANTMAN, *Nonlinear Problems of Elasticity (Second Edition)*, Springer, New York, 2004.
 494 [2] C. BLONDEL, R. VAILLANT, G. MALANDAIN, AND N. AYACHE, *3d tomographic reconstruction of*
 495 *coronary arteries using a precomputed 4d motion field*, *Physics in Medicine and Biology*,
 496 49 (2004), pp. 2197–2208.
 497 [3] V. BOUTCHKO, R. RAYZ, N. VANDEHEY, J. O’NEIL, T. BUDINGER, P. NICO, AND W. MOSES,
 498 *Imaging and modeling of flow in porous media using clinical nuclear emission tomography*

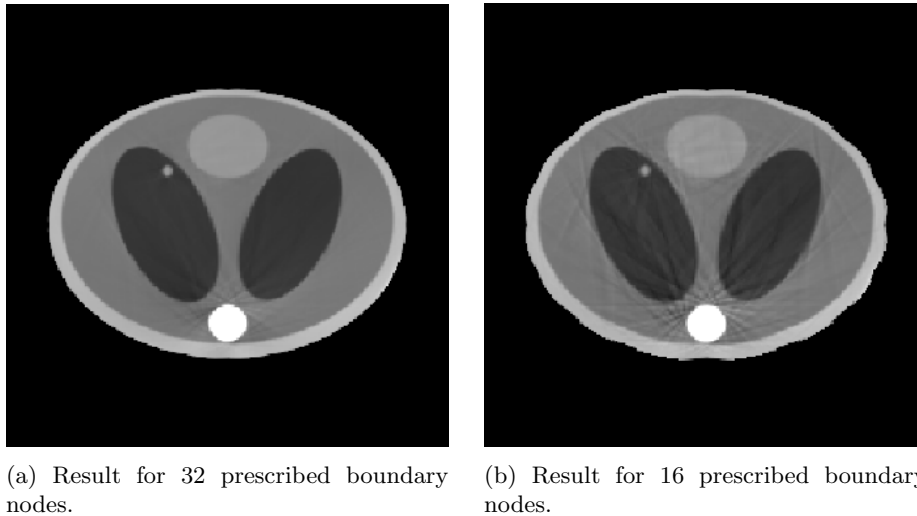


Figure 9: Dynamic reconstruction results with motion information from solving the PDE with only a small number of boundary nodes.

- 499 *systems and computational fluid dynamics*, Journal of Applied Geophysics, 76 (2012),
500 pp. 74–81.
- 501 [4] M. BURGER, H. DIRKS, L. FRERKING, A. HAUPTMANN, T. HELIN, AND S. SILTANEN, *A*
502 *variational reconstruction method for undersampled dynamic x-ray tomography based on*
503 *physical motion models*, Inverse Problems, 33 (2017), p. 124008.
- 504 [5] M. BURGER, H. DIRKS, AND C.-B. SCHÖNLIEB, *A variational model for joint motion estimation*
505 *and image reconstruction*, SIAM Journal on Imaging Sciences, 11 (2018), pp. 94–128.
- 506 [6] C. CHEN, B. GRIS, AND O. ÖKTEM, *A new variational model for joint image reconstruction*
507 *and motion estimation in spatiotemporal imaging*, SIAM J. Imaging Sciences, 12 (2019),
508 pp. 1686–1719.
- 509 [7] C. CHEN AND W. VON WAHL, *Das rand-anfangswertproblem für quasilineare wellengleichungen*
510 *in sobolevräumen niedriger ordnung*, Journal für die reine und angewandte Mathematik,
511 (1982), pp. 77–112.
- 512 [8] J. CHUNG AND L. NGUYEN, *Motion estimation and correction in photoacoustic tomographic*
513 *reconstruction*, SIAM J. Imaging Sci., 10 (2017), pp. 216–242, [https://doi.org/10.1137/](https://doi.org/10.1137/16M1082901)
514 [16M1082901](https://doi.org/10.1137/16M1082901), <https://doi.org/10.1137/16M1082901>.
- 515 [9] J. CHUNG, A. K. SAIBABA, M. BROWN, AND E. WESTMAN, *Efficient generalized golub-kahan*
516 *based methods for dynamic inverse problems*, Inverse Problems, 34 (2018), p. 024005.
- 517 [10] P. G. CIARLET, *Mathematical Elasticity, Vol. I: Three-Dimensional Elasticity*, NH, 1988.
- 518 [11] C. CRAWFORD, K. KING, C. RITCHIE, AND J. GODWIN, *Respiratory compensation in projection*
519 *imaging using a magnification and displacement model*, IEEE Transactions on Medical
520 Imaging, 15 (1996), pp. 327–332.
- 521 [12] L. DESBAT, S. ROUX, AND P. GRANGEAT, *Compensation of some time dependent deformations*
522 *in tomography*, IEEE Transactions on Medical Imaging, 26 (2007), pp. 261–269.
- 523 [13] J. FITZGERALD AND P. DANIAS, *Effect of motion on cardiac spect imaging: Recognition and*
524 *motion correction*, Journal of Nuclear Cardiology, 8 (2001), pp. 701–706.
- 525 [14] F. GIGENGACK, L. RUTHOTTO, M. BURGER, C. WOLTERS, X. JIANG, AND K. SCHÄFFERS, *Motion*
526 *correction in dual gated cardiac pet using mass-preserving image registration*, IEEE Trans.
527 Med. Imag., 31 (2012), pp. 698–712.
- 528 [15] E. GRAVIER, Y. YANG, AND M. JIN, *Tomographic reconstruction of dynamic cardiac image se-*
529 *quences*, IEEE Transactions on Image Processing, 16 (2007), p. 932–942.
- 530 [16] B. HAHN, *Reconstruction of dynamic objects with affine deformations in dynamic computerized*
531 *tomography*, J. Inverse Ill-Posed Probl., 22 (2014), pp. 323–339.
- 532 [17] B. N. HAHN, *Efficient algorithms for linear dynamic inverse problems with known motion*,

- 533 Inverse Problems, 30 (2014), pp. 035008, 20.
- 534 [18] B. N. HAHN, *Motion estimation and compensation strategies in dynamic computerized*
535 *tomography*, Sensing and Imaging, 18 (2017), pp. 1–20.
- 536 [19] B. N. HAHN AND M.-L. KIENLE GARRIDO, *An efficient reconstruction approach for a class of*
537 *dynamic imaging operators*, Inverse Problems, 35 (2019), p. 094005.
- 538 [20] B. N. HAHN, M.-L. KIENLE GARRIDO, AND E. T. QUINTO, *Microlocal properties of dynamic*
539 *Fourier integral operators*, in Time-dependent Problems in Imaging and Parameter
540 Identification, B. Kaltenbacher, T. Schuster, and A. Wald, eds., Springer Verlag, to appear.
- 541 [21] B. N. HAHN AND E. T. QUINTO, *Detectable singularities from dynamic radon data*, SIAM
542 Journal on Imaging Sciences, 9 (2016), pp. 1195–1225.
- 543 [22] L. HÖRMANDER, *The analysis of linear partial differential operators IV: Fourier Integral*
544 *Operators*, Springer, 2009.
- 545 [23] T. HUGHES, T. KATO, AND J. MARSDEN, *Well-posed quasilinear second-order hyperbolic systems*
546 *with applications to nonlinear elastodynamics and general relativity*, Arch. Rational Mech.
547 Anal., 63 (1977), pp. 273–294, <https://doi.org/https://doi.org/10.1007/BF00251584>.
- 548 [24] A. ISOLA, A. ZIEGLER, T. KOEHLER, W. NIESSEN, AND M. GRASS, *Motion-compensated*
549 *iterative cone-beam ct image reconstruction with adapted blobs as basis functions*, Physics
550 in Medicine and Biology, 53 (2008), pp. 6777–6797.
- 551 [25] J. KASTNER, B. PLANK, AND C. HEINZL, *Advanced x-ray computed tomography methods: High*
552 *resolution ct, phase contrast ct, quantitative ct and 4dct*, in Digital Industrial Radiology
553 and Computed Tomography (DIR 2015), Ghent, Belgium, 2015.
- 554 [26] A. KATSEVICH, *An accurate approximate algorithm for motion compensation in two-*
555 *dimensional tomography*, Inverse Problems, 26 (2010), pp. 065007, 16, [https://doi.org/](https://doi.org/10.1088/0266-5611/26/6/065007)
556 [10.1088/0266-5611/26/6/065007](https://doi.org/10.1088/0266-5611/26/6/065007), <http://dx.doi.org/10.1088/0266-5611/26/6/065007>.
- 557 [27] A. KATSEVICH, *A local approach to resolution analysis of image reconstruction in tomography*,
558 SIAM J. Appl. Math., 77 (2017), p. 1706–1732, <https://doi.org/10.1137/17M112108>.
- 559 [28] A. KATSEVICH, M. SILVER, AND A. ZAMYATIN, *Local tomography and the motion estimation*
560 *problem*, SIAM J. Imaging Sci., 4 (2011), pp. 200–219, <https://doi.org/10.1137/100796728>,
561 <http://dx.doi.org/10.1137/100796728>.
- 562 [29] S. KINDERMANN AND A. LEITÃO, *On regularization methods for inverse problems of dynamic*
563 *type*, Numerical Functional Analysis and Optimization, 27 (2006), pp. 139–160.
- 564 [30] V. P. KRISHNAN AND E. T. QUINTO, *Microlocal Analysis in Tomography*, in Handbook of
565 Mathematical Methods in Imaging, O. Scherzer, ed., Springer Verlag, 2015.
- 566 [31] D. LE BIHAN, C. POUPON, A. AMADON, AND F. LETHIMONNIER, *Artifacts and pitfalls in*
567 *diffusion mri*, Journal of Magnetic Resonance Imaging, 24 (2006), pp. 478–488.
- 568 [32] J. LIU, X. ZHANG, X. ZHANG, H. ZHAO, Y. GAO, D. THOMAS, D. LOW, AND H. GAO, *5d*
569 *respiratory motion model based image reconstruction algorithm for 4d cone-beam computed*
570 *tomography*, Inverse Problems, 31 (2015), p. 115007.
- 571 [33] W. LU AND T. R. MACKIE, *Tomographic motion detection and correction directly in sinogram*
572 *space*, Tomographic motion detection and correction directly in sinogram space, 47 (2002),
573 pp. 1267–1284.
- 574 [34] D. MANKE, K. NEHRKE, AND P. BÖRNERT, *Novel prospective respiratory motion correction*
575 *approach for free-breathing coronary mr angiography using a patient-adapted affine motion*
576 *model*, Magnetic Resonance in Medicine, 50 (2003), pp. 122–131.
- 577 [35] F. NATTERER, *The mathematics of computerized tomography*, B. G. Teubner, Stuttgart, 1986.
- 578 [36] F. NATTERER AND F. WÜBBELING, *Mathematical methods in image reconstruction*, SIAM
579 Monographs on Mathematical Modeling and Computation, Society for Industrial and
580 Applied Mathematics (SIAM), Philadelphia, PA, 2001.
- 581 [37] R. OTAZO, E. CANDÈS, AND D. SODICKSON, *Low-rank plus sparse matrix decomposition for*
582 *accelerated dynamic mri with separation of background and dynamic components*, Magnetic
583 Resonance in Medicine, 73 (2015), pp. 1125–1136.
- 584 [38] S. RABIENIAHARATBAR, *Invertibility and stability for a generic class of radon transforms with*
585 *application to dynamic operators*, Journal of Inverse and Ill-Posed Problems, 27 (2018),
586 pp. 469–486, <https://doi.org/10.1515/jiip-2018-0014>.
- 587 [39] M. REYES, G. MALANDAIN, P. KOULIBALY, M. GONZÁLEZ-BALLESTER, AND J. DARCOURT,
588 *Model-based respiratory motion compensation for emission tomography image*
589 *reconstruction*, Physics in Medicine and Biology, 52 (2007), pp. 3579–3600.
- 590 [40] U. SCHMITT AND A. LOUIS, *Efficient algorithms for the regularization of dynamic inverse*
591 *problems: I. theory*, Inverse Problems, 18 (2002), pp. 645–658.
- 592 [41] U. SCHMITT, A. LOUIS, C. WOLTERS, AND M. VAUHONEN, *Efficient algorithms for the*
593 *regularization of dynamic inverse problems: Ii. applications*, Inverse Problems, 18 (2002),
594 pp. 659–676.

- 595 [42] L. SHEPP, S. HILAL, AND R. SCHULZ, *The tuning fork artifact in computerized tomography*,
596 *Computer Graphics and Image Processing*, 10 (1979), pp. 246–255.
- 597 [43] R. M. TEMAM AND A. M. MIRANVILLE, *Mathematical Modeling in Continuum Mechanics*
598 *(Second Edition)*, Cambridge University Press, New York, 2005.
- 599 [44] F. TRÈVES, *Introduction to Pseudodifferential and Fourier Integral Operators*, Volume 2:
600 *Fourier Integral Operators*, Plenum Press, New York and London, 1980.
- 601 [45] G. VAN EYNDHOVEN, J. SIJBERS, AND J. BATENBURG, *Combined motion estimation and*
602 *reconstruction in tomography*, *Lecture Notes in Computer Science*, 7583 (2012), pp. 12–21.
- 603 [46] V. VAN NIEUWENHOVE, J. DE BEENHOUWER, T. DE SCHRYVER, L. VAN HOOREBEKE, AND
604 J. SIJBERS, *Data-driven affine deformation estimation and correction in cone beam*
605 *computed tomography*, *IEEE Transactions on Image Processing*, 26 (2017), pp. 1441–1451.
- 606 [47] R. WERNER, *Strahlentherapie atmungsbewegter Tumoren*, Springer Vieweg, Wiesbaden, 2013.
- 607 [48] H. YU AND G. WANG, *Data consistency based rigid motion artifact reduction in fan-beam ct*,
608 *IEEE Transactions on Medical Imaging*, 26 (2007), pp. 249–260.